Journal of Sound and Vibration 450 (2019) 214–230

Contents lists available at ScienceDirect

Journal of Sound and Vibration

journal homepage: www.elsevier.com/locate/jsvi

Flow distortion recorded by sonic anemometers on a long-span bridge: Towards a better modelling of the dynamic wind load in full-scale

Etienne Cheynet [a,*], Jasna Bogunović Jakobsen [a], Jónas Snæbjörnsson [a,b]

[a] Department of Mechanical and Structural Engineering and Materials Science, University of Stavanger, N-4036, Stavanger, Norway
[b] School of Science and Engineering, Reykjavík University, Menntavegur 1, 101, Reykjavík, Iceland

ARTICLE INFO

Article history:
Received 5 October 2018
Revised 26 February 2019
Accepted 11 March 2019
Available online 15 March 2019
Handling Editor: Lixi Huang

Keywords:
Full-scale
Flow distortion
Sonic anemometer
Buffeting theory
Suspension bridge
Complex terrain

ABSTRACT

The turbulent wind field around a suspension bridge deck is studied using eleven months of full-scale records from sonic anemometers mounted above the girder. Using the mean and turbulent velocity characteristics, we demonstrate that the bridge structure can significantly distort the flow. More precisely, the friction velocity, the variance of the fluctuating vertical velocity and the mean wind incidence angle are underestimated on the downstream side of the deck. The local topography is also found to influence the flow in a non-negligible way, such that turbulence characteristics differ significantly from those observed in flat and homogeneous terrains. For a hexagonal girder with a width to height ratio $B/H \approx 4.5$, deck-induced flow distortion is still observed on the downwind side of the girder at a height above the road equal to $3.6H$. This further supports the idea that wind measurements from a suspension bridge should rely on anemometers on both sides of the deck to mitigate flow distortion. The improved flow description combined with high-resolution acceleration records of the deck provides a simulation of the wind-induced response of the bridge with a level of accuracy that is rarely achieved in full-scale. In particular, the limits of a wind model based on flat terrain assumption as well as the limits of the strip theory are highlighted by the recorded data and the improved modelling of the bridge buffeting response.

1. Introduction

Measurements of wind turbulence above the deck of long-span cable-suspended bridges in full-scale can be traced back to the 1970s [1,2]. The data gathered this way can be used to model the dynamic wind load acting on the deck [3–8], as well as to conveniently study the horizontal structure of atmospheric turbulence without deploying multiple met-masts. However, the possible flow distortion caused by the bridge deck has rarely been studied in details. Jensen and Hjort-Hansen [1] noted for the case of the Sotra suspension bridge (Norway), which has a truss girder, that the anemometer records collected 3 m above the upwind side of the deck were influenced by the bridge structure. This influence was, however, assumed small enough to be neglected. They found an average incidence angle of 7° and the turbulence statistics were thus studied in the streamline coordinate system, i.e. in a coordinate system where the vertical mean wind speed is as close as possible to 0 ms^{-1}. Hay [3,9] estimated the power spectral density (PSD) of the along-wind and vertical velocity components at two positions above

* Corresponding author.
E-mail address: etienne.cheynet@uis.no (E. Cheynet).

https://doi.org/10.1016/j.jsv.2019.03.013

the Erskine Bridge (UK), which has a 31m-wide and 3.2m-high trapezoidal deck. The first position was on a 7m-high boom on the upwind side of the deck, whereas the second one was on a 9m-high lamp standard near the middle part of the deck, widthwise. For the latter sensor, Hay [3] found that the vertical velocity spectrum was clearly distorted, whereas the along-velocity spectrum was much less affected by the presence of the girder. Frandsen [10] used finite element flow simulations to access the expected flow disturbances by the Great Belt East suspension bridge deck. The analysis, considering the deck without the railings, indicated that the cup anemometer installed 2.3 m above the upwind side of the deck was expected to be located in the undisturbed mean free-stream velocity region. On the downwind side, a height of 2 m was considered sufficient.

The aforementioned observations underline the complex influence of the deck geometry on the flow measured by anemometers. They also reflect the need for improved understanding of flow distortion by a bridge deck in full-scale for a better modelling of the wind forces acting on the structure. Since 2013, the Lysefjord suspension bridge (Norway) has been used as a full-scale laboratory to study the wind effects on a long-span bridge in complex terrain [11]. Since July 2017, the flow has been recorded by nine sonic anemometers installed on both the upwind and downwind sides of the girder, whereas four pairs of accelerometers monitor the deck vibrations. Using eleven months of atmospheric measurements and full-scale acceleration records, from July 2017 through May 2018, we investigate the bridge girder influence on the flow across the deck and the associated wind-induced response.

Flow distortion is here defined as the deviation of wind velocity characteristics from those estimated in flat and homogeneous terrain with an infinite fetch. Therefore, we distinguish between girder-induced flow distortion and terrain-induced flow distortion, often referred to as “orography” effects. An additional distortion of the recorded turbulence signal originates in the interaction between anemometer geometry and the flow through the sensor head. This “sensor-induced flow distortion” refers to both the shadowing effect of the transducer and the flow interruption of the frame of the anemometer. The sensor-induced flow distortion leads to an angle of attack error that is usually reduced using an appropriate calibration [12] but that can still be non-negligible under highly turbulent conditions [13].

The present paper is organized as follows: In section 2, the bridge instrumentation and the data post-processing are presented. section 3 compares the turbulence characteristics estimated using the sonic anemometers on both the upwind and downwind sides of the girder. section 4 assesses how the sonic anemometer position affects the computed bridge response and discusses the limits of the strip assumption from a full-scale perspective.

2. Instrumentation and methods

2.1. Bridge instrumentation

The Lysefjord bridge is a suspension bridge with a main span of 446 m, crossing the inlet of a narrow and long fjord with an azimuth of −42° (Fig. 1). The fjord is enclosed by mountains and steep hills that channel the flow, such that two main wind directions are primarily observed. The first sector corresponds to a flow from north-northeast, i.e. from the inside of the fjord, at azimuth between 0° and 60°. The second one corresponds to a flow from south-southwest, i.e. a wind direction between 180° and 270°.

The Lysefjord bridge has been instrumented with a wind and structural health monitoring system since November 2013 [11]. In June 2017, the arrangement of the wind sensors was modified and three sonic anemometers were installed on the east side of the bridge. In Fig. 2, the position of the anemometers above the deck is defined using the hanger name H*XY*, where *X* is a digit between 08 and 24 indicating the hanger number, and *Y* denotes the west side (W) or east side (E) of the deck. Since two anemometers are mounted on the west hanger no. 08 (H08W), the notations H08Wb and H08Wt refer to the sonic anemometer mounted 6 m (bottom) and 10 m (top) above the deck, respectively. Eight of the sonic anemometers are 3-D WindMaster Pro from Gill instruments (Lymington, UK), which can operate with a sampling frequency up to 32 Hz. The last sonic anemometer, mounted on H10W, is a Weather Transmitter WXT520 from Vaisala (Helsinki, Finland), which monitors the horizontal wind components, rainfall, relative humidity, pressure and absolute temperature with a sampling frequency up to 4 Hz.

Four pairs of tri-axial accelerometers (CUSP-3D from Canterbury Seismic Instruments) are installed inside the deck, near hangers H-09, H-18, H-24 and H-30. Each pair can operate with a sampling frequency up to 200 Hz and is mounted on both sides of the deck so that the vertical and torsional bridge responses can be studied separately. The data are recorded in groups, by five acquisition units. A master data logging unit synchronizes all the data into a single file, which is then continuously transmitted via a mobile network.

2.2. Data processing

The along-wind, crosswind and vertical wind velocity components are denoted u, v and w (positive z-axis), respectively. Each component is expressed as the sum of a mean component, denoted by an overbar, and a fluctuating component with zero mean denoted by a prime, defined as a Gaussian stationary random process, such that for $j = \{u, v, w\}$, one can write $j = \overline{j} + j'$.

The sonic anemometers deployed on the Lysefjord bridge continuously monitor the flow and the amount of data gathered is, therefore, enormous. The data post-processing is done as follows:

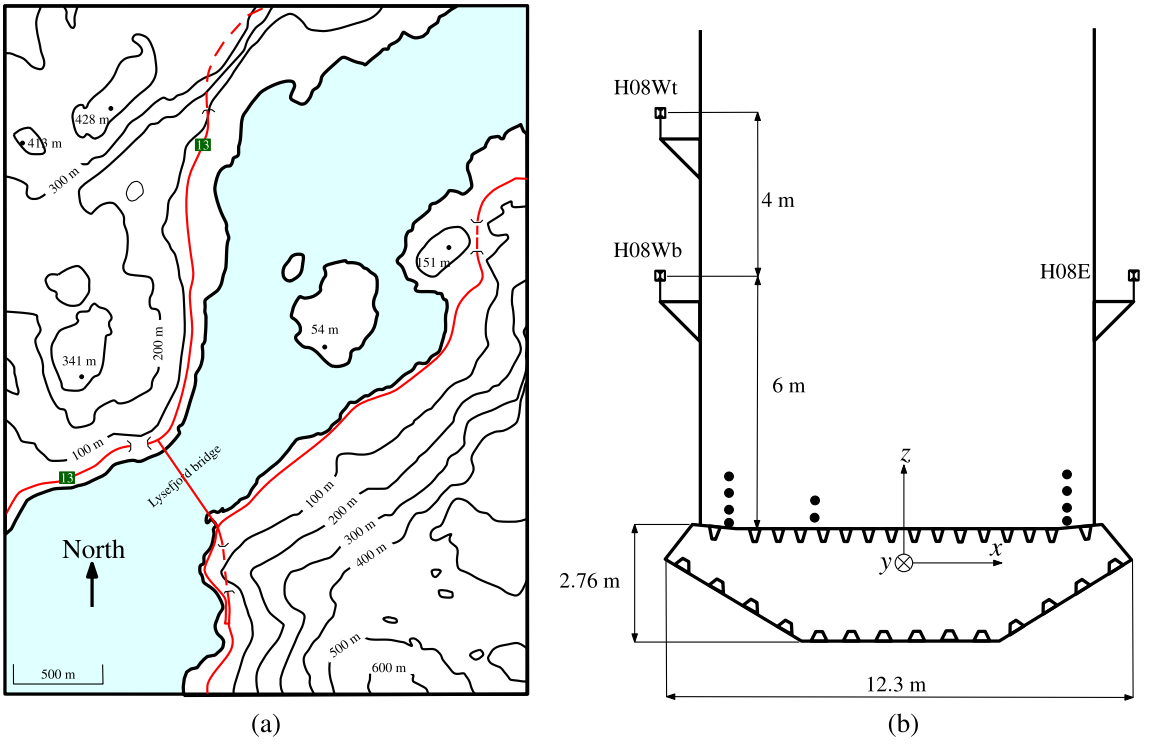

Fig. 1. (a) Topographic map of the Lysefjord bridge. (b) sketch of the cross-section of the Lysefjord bridge deck on hanger 08.

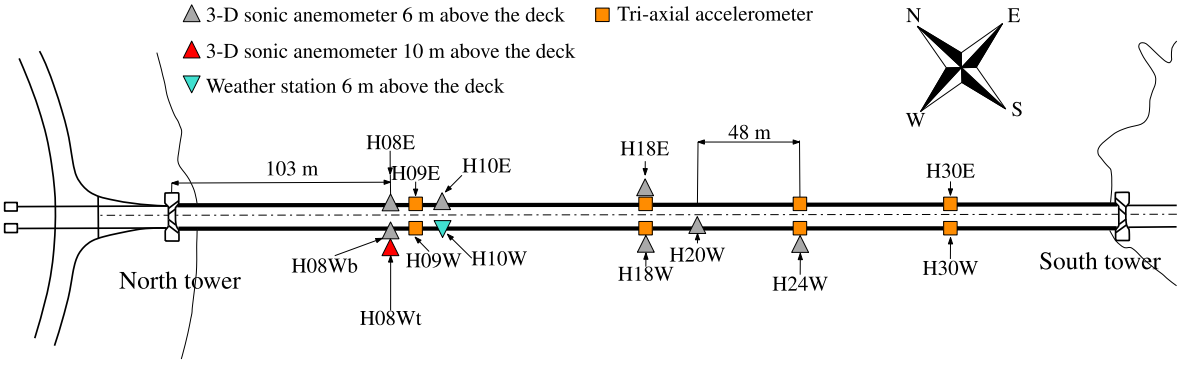

Fig. 2. Instrumentation of the Lysefjord bridge since June 2017. The distance between each hanger is 12 m.

(a) time series are de-spiked and decimated down to a frequency of 25 Hz to facilitate data handling.
(b) Unphysical signals characterized by an absolute value of the skewness above 2 or a kurtosis above 8 are dismissed [14,15].
(c) The underestimation of the vertical wind velocity component due to angle of attack errors [13] is corrected during the post-processing of the data using the correction provided by Gill Instrument, which is a multiplication scaling factor. Note that the anemometers located on H08E and H10E, are new, from an updated production lot, and do not need such a correction.
(d) The coordinate system is rotated such that $\overline{v} \approx \overline{w} \approx 0$. The study in such a coordinate system can be done using the planar-fit (PF) algorithm [16,17], the double rotation method or triple rotation method [18]. In the present case, the high complexity of the terrain justifies the application of the double rotation technique rather than a sectoral PF algorithm, which may have a limited applicability in such an environment [19].
(e) Non-stationary samples are omitted in the further analysis as well as those associated with a mean wind speed below 6 m s^{-1}. Only the second-order stationarity is considered here, i.e. the time-dependency of statistical moments up to order two. For each time series, the centred moving mean and moving standard deviation are studied, using a half window length of 5min. If a local deviation from the mean or standard deviation greater than 40% is detected, the time series

is assumed non-stationary and dismissed. The values of the threshold parameters and window length have been chosen using simulated stationary turbulent wind velocity histories that are generated using the method by Shinozuka and Deodatis [20], which showed that such a choice was appropriate to differentiate between the random error, due to the finite averaging time, and the error due to non-stationary fluctuations.

(f) Following Stiperski and Rotach [15], the measurement uncertainties in the variance and covariance of the wind velocity records are assessed. For the wind velocity component $j = \{u, v, w\}$, the measurement uncertainty a_j for the variance is defined as,

$$a_{jj}^2 = \frac{4z}{\tau \overline{u}(z)} \left[\kappa_j - 1\right] \tag{1}$$

where τ is the averaging time; κ_j is the kurtosis of the velocity component j and $\overline{u}(z)$ is the mean wind speed at a height z above the ground. Similarly, the measurement uncertainty for the covariance $\overline{u'w'}$ and $\overline{v'w'}$ between the horizontal and vertical velocity components are defined as:

$$a_{uw}^2 = \frac{z}{\tau \overline{u}(z)} \left[\frac{\overline{(u'w')^2}}{u_*^4} - 1 \right] \tag{2}$$

$$a_{vw}^2 = \frac{z}{\tau \overline{u}(z)} \left[\frac{\overline{(v'w')^2}}{u_*^4} - 1 \right] \tag{3}$$

where u_* is the friction velocity, calculated as advised by Weber [21]:

$$u_* = \left(\overline{u'w'}^2 + \overline{v'w'}^2 \right)^{1/4} \tag{4}$$

As eqs. (1)–(3) show, the measurement uncertainty is affected by the time series duration. Longer time series should reduce the measurement uncertainties but also increase the number of non-stationary records, thereby reducing the amount of suitable data for the analysis. Therefore, a duration of 30min was found better suited to collect a larger number of high-quality data. For that averaging time, the median value of a_{ii}, where $i, j = \{u, v, w\}$, is ca. 20% whereas the median value for a_{uw} and a_{vw} is around 33%. Samples associated with a measurement uncertainty above 50% are disregarded as advised by Stiperski and Rotach [15], which accounts for ca. 8% of samples with a mean wind speed above 6 ms^{-1}.

(g) Turbulence characteristics are studied after removing the mean and any linear trend from the approved time series.

The atmospheric stability is estimated using the non-dimensional Obukhov length ζ, local scaling [22,23] and assuming that the virtual potential temperature is well approximated by the sonic temperature:

$$\zeta = \frac{-g\kappa z \overline{w'\theta_v'}}{\overline{\theta_v} u_*^3} \tag{5}$$

where $g = 9.81\ \mathrm{m\ s}^{-2}$ is the acceleration of gravity; $\overline{\theta_v}$ is the average virtual potential temperature; $\overline{w'\theta_v'}$ is the flux of virtual potential temperature and $\kappa \approx 0.4$ is the von Kármán constant. Only samples characterized by $|\zeta| < 0.1$, which represents near-neutral conditions, are considered in the following.

The one-point power-spectral density (PSD) estimates of the velocity fluctuations are denoted S_j, where $j = \{u, v, w\}$, and are computed using the periodogram method with a Hamming window. The periodogram method is generally associated with a large random error, which is reduced by block-averaging each individual spectra into 60 bins equally spaced on a logarithmic scale. Then, each PSD estimate is normalized and ensemble averaged. As the record duration is 30min, the lowest frequency recorded is 0.56 mHz. The real part of the normalized cross-spectrum, called co-coherence, is estimated using Welch's algorithm [24] with a Hamming window, six segments and 50% overlapping.

In addition to the one-point velocity spectra and cross-spectra, the turbulence intensity I_j, where $j = \{u, v, w\}$, is studied at wind velocities large enough so that I_j produce stable values. We recall that I_j is defined as

$$I_j(z) = \frac{\sigma_j(z)}{\overline{u}(z)} \tag{6}$$

where σ_j is the standard deviation of the velocity component j.

2.3. Wind load and bridge response modelling

The action of atmospheric turbulence on a wind-sensitive structure is named buffeting load and the associated dynamic response is named buffeting response [25,26]. The frequency domain approach, which relies on the computation of the power spectral density and the associated standard deviation of the bridge displacement and/or acceleration response is considered in the following. If the flow is not perpendicular to the bridge longitudinal axis, it is said "skewed". The angle between the normal

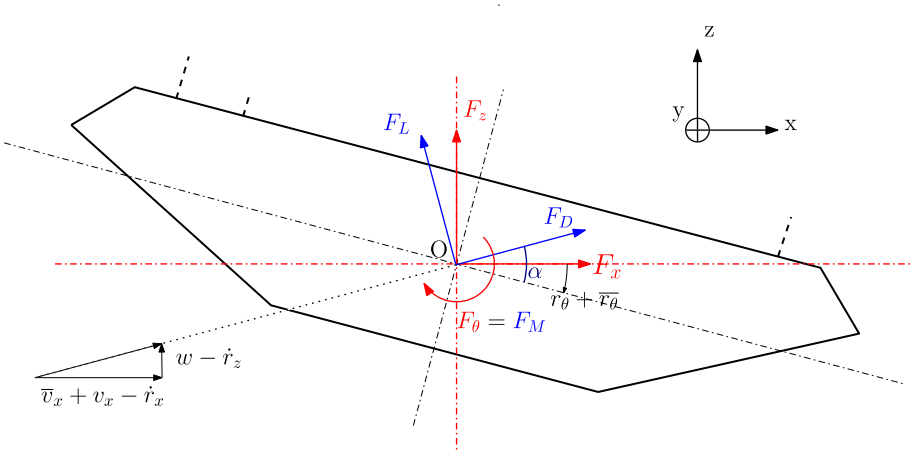

Fig. 3. Wind load components acting on the cross section of the bridge girder, where F_x, F_z, F_D, F_L and F_M refer to the horizontal load, the vertical load, the drag, the lift and the overturning moment, respectively. The deck lateral, vertical and torsional displacement responses are written r_x, r_z and r_θ, respectively, whereas α is the angle of attack.

to the deck and the wind direction is the "yaw angle" β. The horizontal wind velocity component normal to the deck is here denoted v_x,

$$v_x = u\cos(\beta) + v\sin(\beta) \tag{7}$$

In the present study, only the vertical bridge acceleration response is computed, which for simplicity is evaluated using the vertical wind velocity component only. This relies on the assumption that the fluctuating horizontal velocity components have a negligible influence on the dynamic vertical bridge response, which is generally verified for the wind conditions recorded on the Lysefjord bridge site [27, p. 146]. The buffeting response of the Lysefjord bridge is computed using the quasi-steady assumption, i.e. assuming that the flow instantaneously adapts to the moving bridge deck such that the aerodynamic coefficients and their first derivative are independent of the frequency. The aerodynamic forces are linearised with respect to the time-dependent angle of attack, using Taylor series up to order 1. As shown in Cheynet et al. [28], the linearisation of the buffeting load is justified for the study of the vertical bridge response, even under highly turbulent conditions. Modal coupling effects are neglected as the wind velocities studied are not high enough to generate significant coupling effects. Finally, the strip assumption is used, i.e. the correlation of the wind forces along and across the bridge deck is taken to be identical to that of the undisturbed, incoming wind fluctuations, implying that the cross-sectional aerodynamic admittance is equal to one at every frequency.

The wind load components acting on the bridge deck are summarized in Fig. 3. The mean lift coefficient of the Lysefjord bridge deck at zero angle of attack is $C_L = 0.1$. This low value implies the contribution of the along-wind component to the vertical load becomes negligible compared to the effect of the vertical velocity fluctuations. Therefore, the power spectral density of the turbulent vertical wind load on the bridge deck [28, eqs. (5)–(10)] can be simplified as

$$S_q(y_i, y_j, f) = \left[\frac{1}{2}\rho\overline{v_x}B\left(C_L' + \frac{H}{B}C_D\right)\right]^2 \sqrt{S_w(y_i,f)\cdot S_w(y_j,f)}\cdot\gamma_w(y_i,y_j,f), \tag{8}$$

where $\overline{v_x}$ is the horizontal mean wind velocity component normal to the span; $B = 12.3$ m and $H = 2.76$ m are the girder width and height, respectively. Whereas the lift coefficient refers to the deck width B, the drag coefficient is defined using the deck height H. The first derivative of the deck lift coefficient with respect to the incidence angle is $C_L' = 3.0$; $C_D = 1.0$ is the bridge deck drag coefficient; $S_w(y_i,f)$ is the vertical velocity spectrum at the coordinate y_i and $\gamma_w(y_i,y_j,f)$ is the along-span co-coherence of the vertical velocity component between the coordinates y_i and y_j. The co-coherence is affected by the yaw angle, as studied by e.g. Xie et al. [29]. In the present case, the yaw angle is accounted for in the expression of γ_w using the crosswind separation instead of the along-span separation, as done previously by e.g. Saranyasoontorn et al. [30].

The spectrum of the modal wind load $\boldsymbol{S}_Q$ is associated with the mode shapes $\boldsymbol{\Phi}(y)$ of the bridge deck, on which the buffeting load is concentrated,

$$\boldsymbol{S}_Q(f) = \int_0^L\int_0^L \boldsymbol{\Phi}(y_i)S_q(y_i,y_j,f)\boldsymbol{\Phi}(y_j)\mathrm{d}y_i\mathrm{d}y_j. \tag{9}$$

The power spectral density of the bridge response is

$$S_{r_z}(y,f) = \left[\boldsymbol{\Phi}(y)\cdot\boldsymbol{H}(f)\right]\cdot\boldsymbol{S}_Q(f)\cdot\left[\boldsymbol{\Phi}(y)\cdot\boldsymbol{H}(f)\right]^{\mathsf{T}}, \tag{10}$$

where $\boldsymbol{H}(f)$ is the mechanical admittance of the system modified by the modal aerodynamic damping and stiffness. The mode shapes $\boldsymbol{\Phi}(y)$ and eigenfrequencies of the Lysefjord bridge are computed using a continuum bridge model and the Galerkin

method [31,32]. The modal parameters have been validated and/or corrected using an operational modal analysis relying on an automated covariance-driven stochastic subspace identification algorithm [28,33].

The standard deviation of the computed bridge displacement response is denoted $\sigma_{r_z}(y)$ and is computed as

$$\sigma_{r_z}(y) = \sqrt{\int_0^\infty S_{r_z}(y,f)\mathrm{d}f}. \tag{11}$$

The vertical turbulent wind load is modelled using the one-point spectra and coherence estimated at mid-span.

Generally, a single spectral model is desired to describe the velocity spectra on both sides of the deck. However, as the spectra affected by flow distortion may have a flattened spectral peak the following spectral form is adopted:

$$\frac{fS_w(f)}{\sigma_i^2} = \frac{a_1 f_r}{\left(1+b_1 f_r\right)^{5/3}} + \frac{a_2 f_r}{1+b_2 f_r^{5/3}} \tag{12}$$

where a_1, a_2, b_1 and b_2 are parameters to be determined and f_r is the reduced frequency defined as

$$f_r = \frac{fz}{\overline{u}} \tag{13}$$

For a flow perpendicular to the bridge deck, the co-coherence γ_w is often modelled using the Davenport model [34]:

$$\gamma_w(y_i,y_j,f) \approx \exp\left(-Cf|y_j-y_i|/\overline{u}(z)\right), \tag{14}$$

where y_i and y_j are two measurement positions; C is a constant named "decay coefficient" and f is the frequency. For a given mean wind speed and frequency, the co-coherence is here assumed to be a function of the spatial separation $d_y = |y_i - y_j|$ only, such that $\gamma_w(d_y,f) \approx \gamma_w(y_i,y_j,f)$. If the flow is not perpendicular to the bridge longitudinal axis, i.e. if the yaw angle β is different from zero, the along-span separation is replaced by the crosswind separation. To better describe γ_w, we use a three-parameter exponential decay function instead of the Davenport coherence model:

$$\gamma_w(d_y,\beta,f) = \exp\left\{-\left[\frac{d_y\cos(\beta)}{\overline{u}}\sqrt{(c_1 f)^2+c_2^2}\right]\right\}\cos\left(c_3\frac{d_y\cos(\beta)f}{\overline{u}}\right) \tag{15}$$

where c_1, c_2 and c_3 are three decay parameters that improve the capabilities to simulate the observed behaviour. The coefficient c_2 permits the co-coherence to be lower than unity at zero frequency, which reflects the finite spatial dimension of the eddies. This is frequently observed for the vertical wind component at large crosswind separations. If c_2 is not introduced, the modelled co-coherence is overestimated at low frequency and underestimated at high frequencies. The parameter c_3 allows the modelled co-coherence to be negative, capturing out-of-phase variations of the wind velocity along the deck due to non-zero yaw angles.

Although the approach adopted above to compute the bridge response is much simpler than in Cheynet et al. [28], it provides a good illustration of the sensitivity of the bridge response to the vertical wind velocity component. In the present study, only wind-induced vibrations are of interest and bridge acceleration records dominated by traffic loading have, therefore, been dismissed. This is achieved by comparing the variance of the low-frequency part of the acceleration spectrum, arbitrarily defined as the range below 1 Hz, with the one from the high-frequency range [27, p. 186–189]. Acceleration samples with a dominant contribution from the high-frequency range are considered to be dominated by traffic-induced vibrations and thus disregarded. Similarly, the possible flow distortion induced by vehicles is assumed negligible in the current study. This is justifiable as the traffic flow rate is generally rather low on the bridge, especially in the cases when wind-induced vibrations are the dominant source of excitation.

3. Results

Fig. 4 displays the mean wind speed and the along-wind turbulence intensity estimated on the Lysefjord bridge from July 2017 to May 2018. The high turbulence intensity recorded, previously mentioned in Cheynet et al. [28], is consistent with measurements from other Norwegian fjords [35]. It suggests that buoyancy-generated turbulence effects are not dominant in the flow. For the period considered, this is also indicated by the stability parameter ζ, for which 61% of the values are bounded between −0.1 and 0.1. The different sonic anemometers give values of ζ that are similar on average, but those corrected for the underestimation of the vertical wind velocity component provide estimates with a considerable scatter, leading to a significant reduction of the data availability. For this reason, the value of ζ used to select samples associated with near-neutral conditions is estimated from the sonic anemometer on H10E only.

Whereas the flow from north-northeast is generally more turbulent than the one from south-southwest, the largest velocities are recorded for the latter sector. Nevertheless, the flow from south-southwest is associated with a turbulence intensity above 0.20 when the wind direction is between 180° and 190°, for which the flow brushes past the west face of the mountain on the south side of the bridge.

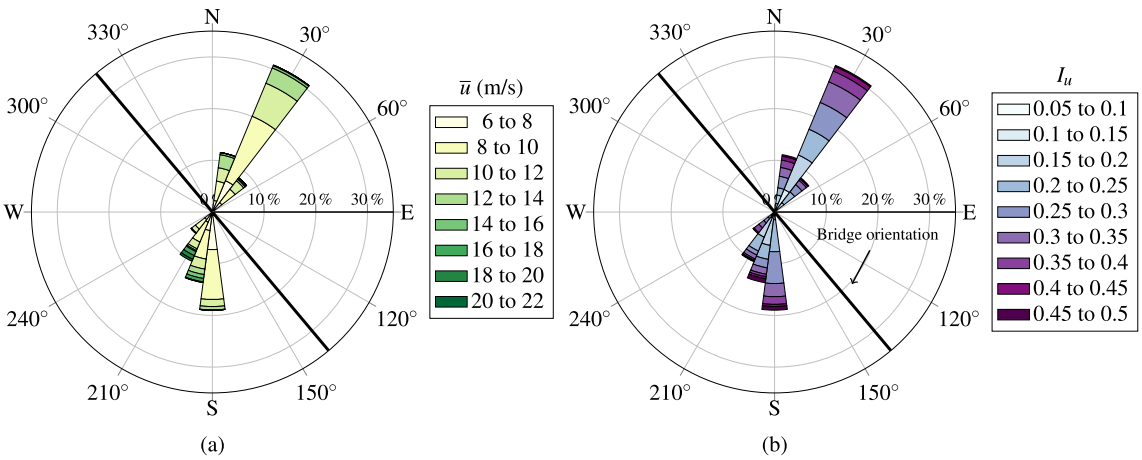

Fig. 4. Mean wind speed (a) and along-wind turbulence intensity (b) recorded from every anemometer on the Lysefjord bridge between July 2017 and May 2018 (1.70×10^3 stationary records of 30min duration with $\overline{u} \geq 6\,\mathrm{m\,s^{-1}}$).

Table 1
Average relative percentage wise difference ϵ_u in the recorded mean wind speed and mean incidence angle α along the deck of the Lysefjord bridge for samples with $\overline{u} \geq 6\,\mathrm{m\,s^{-1}}$ and a 30min averaging time (865 samples for a flow NNE and 697 samples for a flow from SSW).

Sensors		Wind Direction			
West side	East side	south-southwest		north-northeast	
		ϵ_u (%)	$\overline{\alpha}$ (°)	ϵ_u (%)	$\overline{\alpha}$ (°)
H08Wb	–	−0.7	3.5	11.0	−0.4
H08 Wt	–	−0.1	2.9	8.5	−1.1
H10W	–	−1.5	–	12.0	–
H18W	–	0	2.9	2.3	0.1
H20W	–	0.2	1.8	0.5	0.5
H24W	–	−2.4	0.5	−3.4	0.1
–	H08E	1.5	1.2	4.1	0.5
–	H10E	1.0	0.5	2.2	0.8
–	H18E	3.5	0.8	0	3.0

3.1. Mean flow characteristics

A relative difference between the mean wind speed estimated from a reference sonic anemometer and the others, denoted ϵ_u, is investigated in Table 1. The reference sensor is the one located on H18W or H18E for a wind blowing from south-southwest or north-northeast, respectively. Note that the discrepancies due to slightly different measurement heights are not corrected for as the wind shear difference is assumed small. It should also be noted that the anemometer on H10W does not measure the vertical component and, therefore, cannot provide any indication of the wind incidence angle.

For a flow from south-southwest, Table 1 shows that, on average, the absolute relative difference is lower than 4%, indicating that for this particular wind sector the deck has limited influence on the mean flow on the downwind side of the bridge. The larger discrepancies observed between the mean speed measurements on H18W and H24W may be due to terrain-induced flow inhomogeneity. This was previously suggested in Cheynet et al. [36], where lidar measurements indicated the existence of a non-uniform mean flow on the south side of the bridge.

For a flow from north-northeast, the relative difference ϵ_u indicates a stronger flow inhomogeneity than for a flow from south-southwest. Values of ϵ_u larger than 8% on H08Wb and H08 Wt cannot be simply due to the influence of the terrain on the flow. Different flow characteristics from the two wind sectors identified may, however, be responsible for different levels of flow distortion by the bridge deck.

The mean wind incidence angle $\overline{\alpha}$ recorded for the two wind sectors considered are displayed in Table 1 for $\overline{u} \geq 6\,\mathrm{m\,s^{-1}}$. Whereas the south-southwest flow is characterized by $\overline{\alpha} \geq 3°$ on average on the upwind side, which is non-negligible, the sensors located on the downwind side of the deck monitor a lower incidence angle, reflecting a possible influence of the bridge girder on the vertical mean speed recorded 6 m above the road. If a sonic anemometer is not perfectly levelled, a non-zero mean incidence angle is measured. For several anemometers monitoring a horizontal flow, this can lead to incidence angles that have various values if the levelling is slightly different for each sensor. For a flow from north-northeast, which

Table 2
Turbulence characteristics estimated from every sonic anemometer on the Lysefjord bridge, under near-neutral conditions, $\overline{u} > 10\,\mathrm{m\,s^{-1}}$ for a wind direction from south-southwest (SSW) with 88 samples and north-northeast (NNE) with 166 samples.

Sector	Sensor location		$\frac{\sigma_w}{u_*}$	$\frac{\sigma_v}{u_*}$	$\frac{\sigma_u}{u_*}$	$\frac{\sigma_w}{\sigma_u}$	$\frac{\sigma_v}{\sigma_u}$
	West side	East side					
SSW	H08Wb	–	1.82 ± 0.55	2.83 ± 1.20	2.68 ± 0.73	0.71 ± 0.09	1.09 ± 0.22
	H08 Wt	–	1.61 ± 0.30	2.47 ± 0.63	2.39 ± 0.41	0.68 ± 0.08	1.05 ± 0.22
	H10W	–	–	–	–	–	1.04 ± 0.17
	H18W	–	1.85 ± 1.10	2.95 ± 2.00	2.70 ± 1.30	0.69 ± 0.08	1.05 ± 0.23
	H20W	–	1.80 ± 0.56	2.83 ± 1.10	2.61 ± 0.71	0.69 ± 0.07	1.02 ± 0.21
	H24W	–	1.77 ± 0.51	3.01 ± 1.10	2.59 ± 0.65	0.70 ± 0.08	1.07 ± 0.26
	–	H08E	1.46 ± 0.23	2.83 ± 0.61	3.16 ± 0.62	0.49 ± 0.06	0.95 ± 0.17
	–	H10E	1.45 ± 0.20	3.02 ± 0.61	3.11 ± 0.46	0.48 ± 0.05	1.02 ± 0.16
	–	H18E	1.40 ± 0.17	3.00 ± 0.37	3.15 ± 0.49	0.46 ± 0.04	0.98 ± 0.19
NNE	H08Wb	–	1.42 ± 0.37	2.32 ± 0.69	2.91 ± 0.85	0.48 ± 0.04	0.79 ± 0.08
	H08 Wt	–	1.52 ± 0.38	2.14 ± 0.59	2.64 ± 0.74	0.56 ± 0.05	0.79 ± 0.08
	H10W	–	–	–	–	–	0.78 ± 0.09
	H18W	–	1.65 ± 0.67	2.93 ± 1.20	3.53 ± 1.50	0.48 ± 0.04	0.86 ± 0.09
	H20W	–	1.75 ± 0.60	2.88 ± 1.10	3.44 ± 1.20	0.50 ± 0.05	0.85 ± 0.09
	H24W	–	1.60 ± 0.58	2.87 ± 1.00	3.45 ± 1.30	0.45 ± 0.05	0.80 ± 0.08
	–	H08E	1.39 ± 0.30	1.72 ± 0.44	2.05 ± 0.43	0.68 ± 0.06	0.84 ± 0.09
	–	H10E	1.42 ± 0.27	1.76 ± 0.39	2.03 ± 0.39	0.69 ± 0.06	0.86 ± 0.09
	–	H18E	1.53 ± 0.25	1.88 ± 0.33	2.28 ± 0.38	0.67 ± 0.06	0.83 ± 0.08

Table 3
Same as Table 2, but for the turbulence intensity "as seen" by each sensor.

Sector	Sensor location		I_u	I_v	I_w
	West side	East side			
SSW	H08Wb	–	0.14 ± 0.05	0.16 ± 0.16	0.10 ± 0.03
	H08 Wt	–	0.15 ± 0.05	0.16 ± 0.16	0.10 ± 0.03
	H10W	–	0.15 ± 0.05	0.16 ± 0.16	–
	H18W	–	0.15 ± 0.05	0.17 ± 0.17	0.11 ± 0.03
	H20W	–	0.16 ± 0.05	0.17 ± 0.17	0.11 ± 0.03
	H24W	–	0.16 ± 0.05	0.18 ± 0.18	0.11 ± 0.03
	–	H08E	0.16 ± 0.05	0.16 ± 0.16	0.08 ± 0.02
	–	H10E	0.15 ± 0.05	0.16 ± 0.16	0.07 ± 0.02
	–	H18E	0.17 ± 0.04	0.16 ± 0.16	0.08 ± 0.02
NNE	H08Wb	–	0.23 ± 0.07	0.18 ± 0.18	0.11 ± 0.03
	H08 Wt	–	0.22 ± 0.07	0.18 ± 0.18	0.13 ± 0.04
	H10W	–	0.25 ± 0.06	0.20 ± 0.20	–
	H18W	–	0.23 ± 0.08	0.19 ± 0.19	0.11 ± 0.03
	H20W	–	0.23 ± 0.08	0.18 ± 0.18	0.12 ± 0.04
	H24W	–	0.22 ± 0.08	0.17 ± 0.17	0.10 ± 0.03
	–	H08E	0.24 ± 0.07	0.20 ± 0.20	0.17 ± 0.05
	–	H10E	0.23 ± 0.07	0.21 ± 0.21	0.17 ± 0.05
	–	H18E	0.24 ± 0.07	0.20 ± 0.20	0.17 ± 0.05

is more horizontal, such levelling imperfections may explain the more heterogeneous values of the incidence angle recorded along the bridge deck. In summary, the study of the mean flow characteristics on both sides of the deck indicates that the vertical mean wind velocity component may be slightly affected by the deck whereas it is not the case for the along-wind component.

3.2. One-point turbulence characteristics

To study integrated turbulence characteristics on the bridge site in a consistent manner, it is important that the turbulence intensity is more or less constant with the mean wind speed and the wind sector selected. As the turbulence intensity was seen to stabilize as the mean wind approached $10\,\mathrm{m\,s^{-1}}$, only samples characterized by $\overline{u} \geq 10\,\mathrm{m\,s^{-1}}$ are considered in the present subsection, although it reduces considerably the number of samples available.

The estimated one-point turbulence characteristics are displayed separately for a wind direction from south-southwest and north-northeast in Tables 2 and 3. The notation $y \pm x$, used in the following, indicates that x is the standard deviation associated with the ensemble-averaged quantity y. These tables show that the discrepancies observed between the upwind and downwind side are particularly important for the w component whereas they are not clearly defined for the horizontal components.

For a south-southwest flow, the ratio σ_w/u_* is slightly lower on the downwind side than on the upwind side, which must be interpreted with caution as the value generally found in the literature in flat terrain ranges from 1.2 to 1.3 [37], whereas it

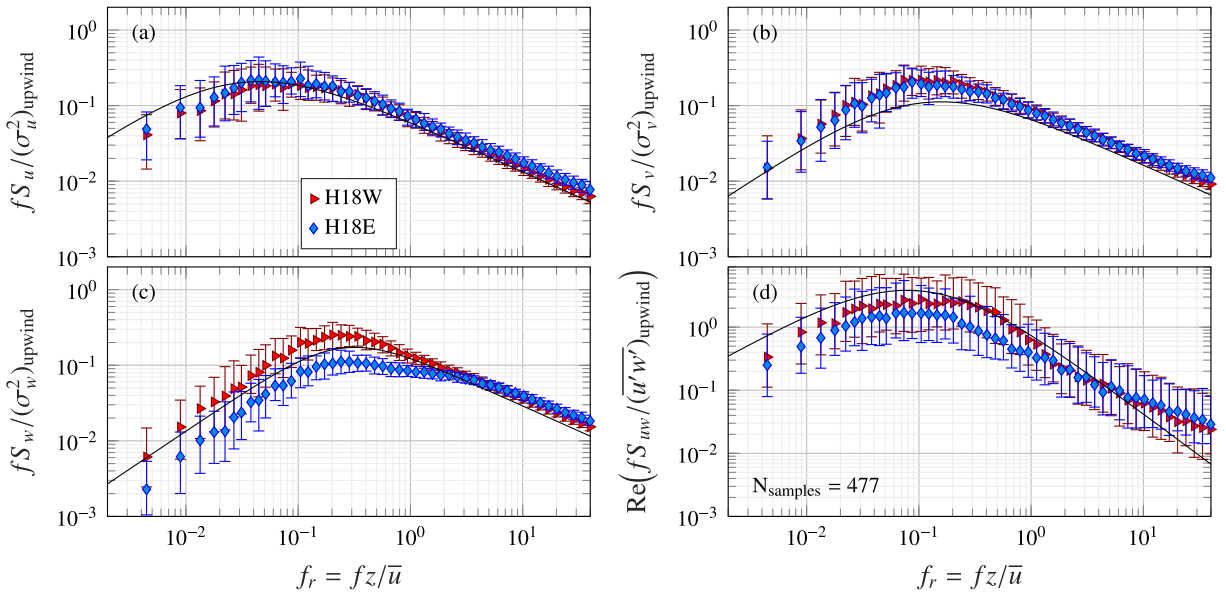

Fig. 5. One-point auto and cross-spectral density estimates from the two sonic anemometers located at mid-span for a flow from south-southwest, near-neutral conditions and $\overline{u} > 6\,\text{m}\,\text{s}^{-1}$ at the deck height (415 samples). The error bar represents the interquartile range and the black solid lines the Kaimal spectral model (a, b, d) and the Busch-Panofsky spectrum (c).

corresponds here to a flow likely distorted by the presence of the deck. Jensen and Hjort-Hansen [1] found a ratio σ_w/u_* between 1.4 and 1.6 on the upwind side of the Sotra Bridge (truss girder), which is consistent with the measurements conducted on the upwind side of the deck for the two wind sectors considered.

The ratio σ_w/σ_u estimated on the upwind side of the bridge is slightly above 0.6, in agreement with Kristensen and Jensen [2], which is larger than the value $\sigma_w/\sigma_u \approx 0.5$, usually found for a flat terrain [38]. On the other hand, only small differences are found for I_u and σ_v/σ_u between the downwind and upwind sides of the bridge deck, indicating that the horizontal components are not significantly affected by flow distortion from the girder. The unusually large ratio $\sigma_v/\sigma_u \approx 1$ obtained for a wind direction from south-southwest may, therefore, be attributed to terrain-induced flow distortion. For a north-northeast flow, a more common value $\sigma_v/\sigma_u \approx 0.8$ is found, although it is still larger than for the Sotra Bridge experiment [2], which was slightly lower than 0.7. The considerable scatter obtained for σ_v/u_* and σ_u/u_*, for both wind directions, may also be attributed to local terrain effects rather than the influence of the bridge structure. Since Table 3 shows that the presence of the deck does not clearly affect I_u, the larger values of σ_u/u_* on the downwind side of the deck are likely caused by an underestimation of u_* due to flow distortion by the girder.

3.3. One-point velocity spectra

Figs. 5 and 6 display the one-point auto and cross spectra normalized by the variance (or covariance) of the velocity estimated on the upwind side of the deck and expressed as a function of the reduced frequency f_r, for a flow from south-southwest and north-northeast, respectively. For the sake of clarity, only the PSD estimates from the sonic anemometers on H18W and H18E are displayed and superimposed to a semi-empirical velocity spectra model, shown as a black solid line. For the two horizontal velocity components and the real part of the cross-spectrum S_{uw}, the Kaimal spectral model [39] is chosen,

$$\frac{fS_u}{u_*^2} = \frac{105 f_r}{\left(1+33 f_r\right)^{5/3}}, \tag{16}$$

$$\frac{fS_v}{u_*^2} = \frac{17 f_r}{\left(1+9.5 f_r\right)^{5/3}}, \tag{17}$$

$$\frac{f\text{Re}\left(S_{uw}\right)}{u_*^2} = -\frac{14 f_r}{\left(1+9.6 f_r\right)^{7/3}}, \tag{18}$$

whereas the Busch-Panofsky spectrum [40] is preferred for the vertical velocity component:

$$\frac{fS_w}{u_*^2} = \frac{3.36 f_r}{1+10 f_r^{5/3}}. \tag{19}$$

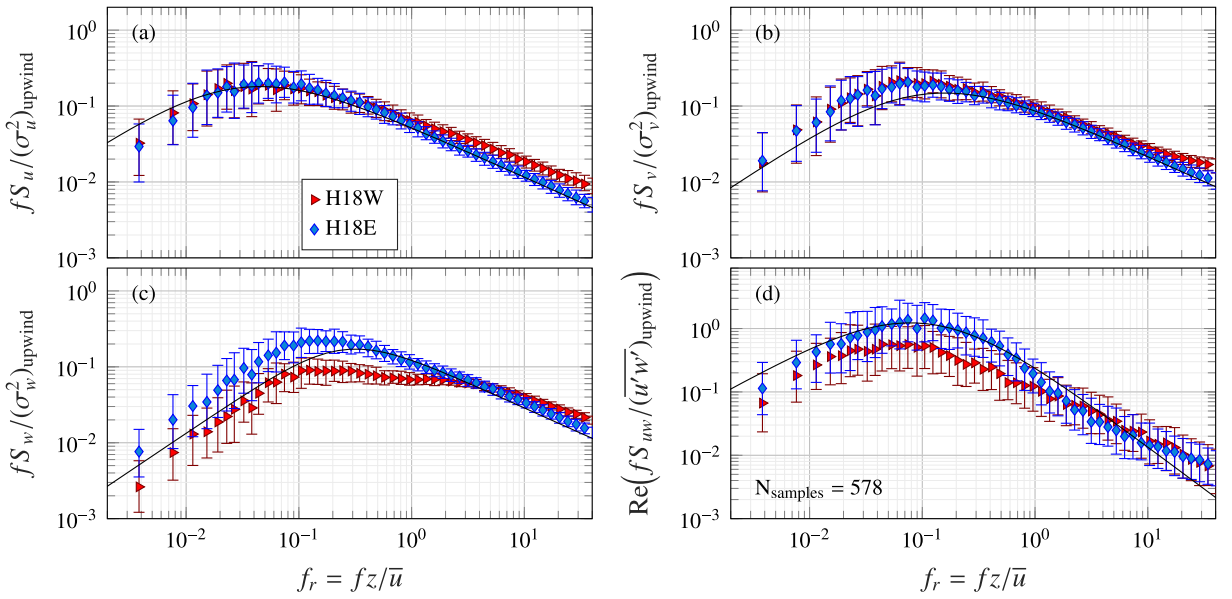

Fig. 6. Same as in Fig. 5 but for a wind blowing from north-northeast (436 samples).

In the field of micro-meteorology, the spectra are generally normalized using the square of the friction velocity whereas, in wind engineering, the variance of the velocity is often preferred. In the present case, the normalization by the velocity variance is applied, using the values displayed in Table 2.

Both figures show that for $0.1 < f_r < 1$, the downwind vertical velocity spectra has a nearly constant value which is considerably lower than the spectral peak of both the reference semi-empirical spectra as well as the upwind spectra. Such behaviour was previously observed by Hay [3] and demonstrates the influence of the bridge deck on the vertical wind velocity component. On the other hand, the two horizontal components show only minor differences between the upwind or downwind side of the girder. Note that for a flow from north-northeast, the S_u spectrum on the downwind side shows values that are slightly larger than on the upwind side for $f_r > 1$, which is also observed for the flow from south-southwest, but to a lower degree. For a turbulent flow past a flat plate, Hunt and Graham [41] predicted an increase of the variance of the horizontal component normal to the plate and a decrease of the variance of the vertical component downwind of the leading edge. While the latter Tables 2 and 3, the increased turbulence for the along-wind component is only visible in the high-frequency range of the PSD estimates, as shown in Figs. 5 and 6 and has no clear consequences on the integrated turbulence characteristics.

For both wind sectors, the co-spectrum estimates from the downwind side of the deck are below those from the upwind side at $f_r < 1$, i.e. at the same reduced frequency as for the S_w spectrum, which can be attributed to the distortion of the flow by the deck. Velocity records from both sides of the deck show, however, discrepancies with the theoretical slope in $-7/3$ of the co-spectrum at $f_r > 3$, implying that the co-spectrum may, in addition, be influenced by the topography upstream of the deck.

3.4. Spectral ratios

The ratio of the PSD estimates of the vertical wind component over the along-wind component are ensemble-averaged and displayed in Fig. 7 for a flow from south-southwest and in Fig. 8 for a flow from north-northeast. Under neutral atmospheric conditions, the theory of local isotropy [42] predicts that the ratio S_w/S_u should reach a value of 1.33 in the inertial subrange, whereas a lower value is expected if the flow is distorted by the bridge deck. On the Sotra bridge (truss girder), Jensen and Hjort-Hansen [1] obtained a ratio S_w/S_u converging adequately toward 1.33 at $f_r > 2$ using sonic anemometers mounted 3 m on the upwind side of the deck, i.e. at a height of 60 m above the sea level, indicating undistorted flow conditions.

Figs. 7 and 8 show that the ratio S_w/S_u obtained using the anemometers located on the downwind side of the bridge is significantly lower than upwind over the entire range of reduced frequencies. If the anemometer data from the upwind side are used, the ratio S_w/S_u converges toward a value ranging from 1.25 to 1.30 at $f_r > 5$, indicating that for a flow from south-southwest, the departure from the local isotropy may be due to a minor flow distortion on the upwind side of the deck, maybe due to the non-zero mean incidence angle. Note that the left panel of Fig. 7 suggests that the flow recorded by the sonic anemometer mounted on H08Wb (6 m above the deck) on the upwind side may be affected, to a limited extent, by the presence of the deck at $0.6 < f_r < 2$. On the other hand, the sensor on H08 Wt (10 m above the deck) does not indicate any influence from the bridge deck when located upwind.

Fig. 8 shows clearly that flow distortion is not uniform along the girder, as it is seen for flow from north-northeast, that the anemometer mounted on the southern part of the bridge records the strongest distortion with a ratio $S_w/S_u \approx 0.8$ at $f_r \approx 10$,

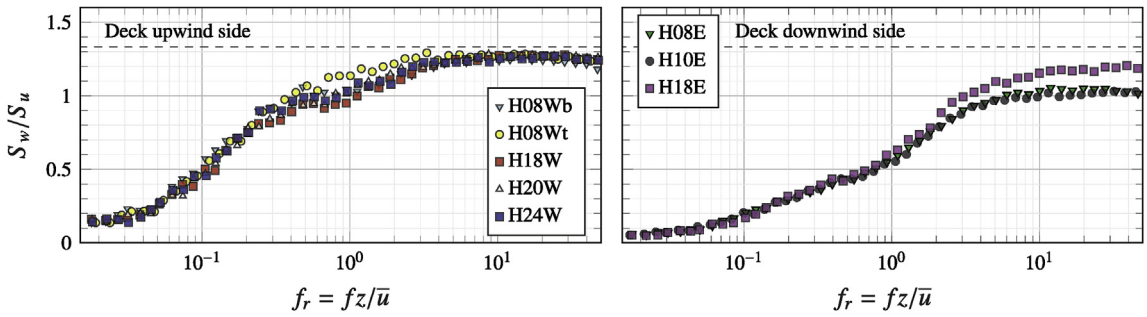

Fig. 7. Ratio of the PSD estimates of the vertical wind component over the along-wind component for a flow from south-southwest, near-neutral conditions and $\overline{u} > 6\,\mathrm{m\,s^{-1}}$ at the deck height (415 samples). The dashed line shows the theoretical ratio of 1.33.

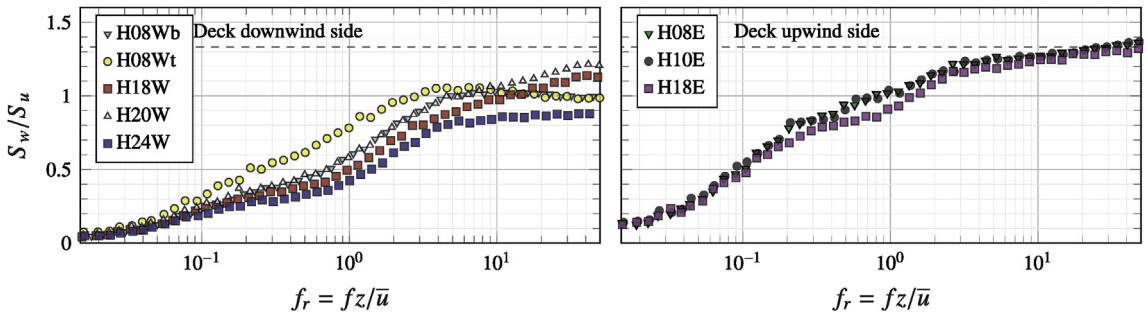

Fig. 8. Same as in Fig. 7 but for a wind blowing from north-northeast (433 samples).

which for $z = 60$ m and $\overline{u} = 10\,\mathrm{m\,s^{-1}}$ corresponds to $f = 1.7$ Hz. Near $f_r \approx 1$, which for $z = 60$ m and $\overline{u} = 10\,\mathrm{m\,s^{-1}}$ corresponds to the first eigenfrequencies of the bridge, the ratio S_w/S_u is also twice as low on the downstream side than on the upwind side, reinforcing the idea that the resonant buffeting response is underestimated if velocity records are gathered on the downstream side only. For a flow from south-southwest (Fig. 7), the three anemometers located on the East side of the bridge show a similar level of flow distortion, except at $f_r > 4$ where the ratio S_w/S_u is smaller on the northern side of the bridge. The non-uniformity of the flow distortion along the span may be due to the large yaw angles recorded, such that the anemometers installed furthest from the initial separation point are located in a more developed turbulent layer. Another contributing factor may also be the asymmetric layout of the bridge girder with respect to its midspan, associated with the 7.5 m altitude difference between the north and south end.

3.5. Wind co-coherence

The ensemble-averaged along-span wind co-coherence for the u and w components is estimated on both the upwind and downwind side of the bridge. The goal is to establish how the coherence is affected by the presence of the girder. Figs. 9 and 10 show such co-coherence estimates, which are evaluated using the same along-span separation lengths for a north-northeast flow and south-southwest one, respectively. Both wind sectors show that the deck is responsible for a slight decrease of the co-coherence on the downstream side, especially at low spatial separations. Nevertheless, this effect is relatively small and is only detectable in the present case because a large amount of samples is used, which allows an efficient smoothing of the coherence estimates.

An equally important challenge is the proper modelling of the co-coherence, as the right panels of Figs. 9 and 10 show that the Davenport model cannot capture efficiently γ_w at large lateral separations since γ_w is substantially lower than unity as the frequency approaches zero. Increasing discrepancies from the Davenport model are expected at $kd_y cos(\beta) < 1$, which for a mean wind speed of 15 $\mathrm{ms^{-1}}$ and a crosswind separation of 20 m, corresponds to frequencies below 0.12 Hz. The latter frequency range coincides with the lowest vibrations modes of suspension bridges with a main span of 1 km or more, calling for an improved modelling of the co-coherence for the wind-resistant design of such structures.

3.6. Influence of the sensor height on turbulence characterization

The results presented in section 3 indicate that every sonic anemometer located on the downstream side of the girder can be affected by bridge-induced flow distortion, even the one mounted 10 m above the deck (H08 Wt). Fig. 11 compares the

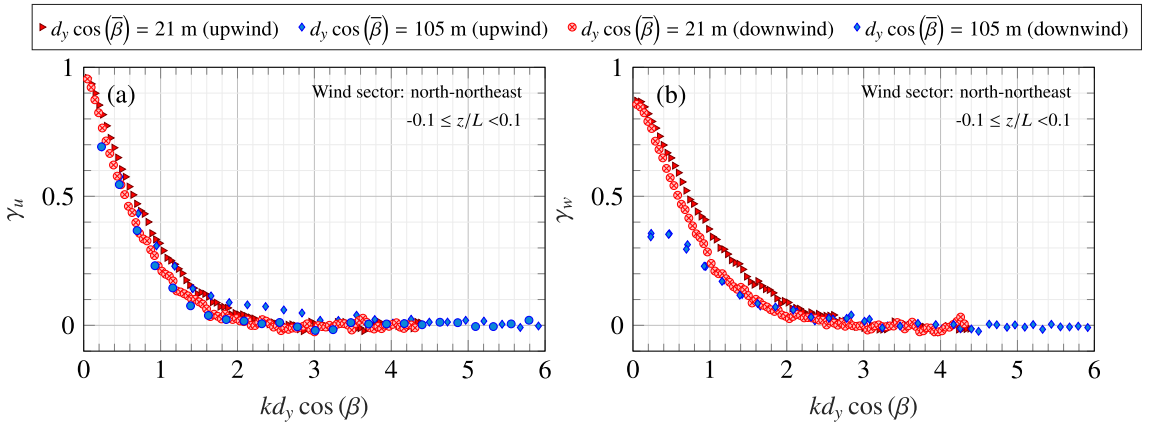

Fig. 9. Along-span co-coherence estimates of the along-wind (a) and vertical (b) velocity components, for a flow from north-northeast, recorded at the upwind and downwind side of the bridge deck (444 samples).

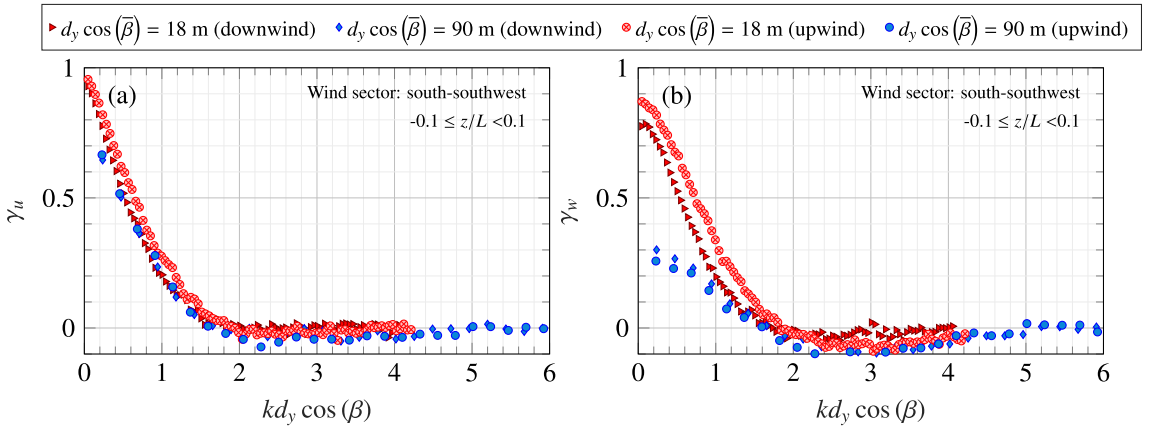

Fig. 10. Same as in Fig. 7 but for a wind blowing from south-south-east (313 samples).

normalized PSD estimates of the vertical wind velocity component on hanger 8, on both sides of the deck. For a flow from north-northeast (left panel of Fig. 11), the two anemometers on the downwind side are those located at the height of 10 m (H08 Wt) and 6 m (H08Wb) above the road, respectively. Their records show a reduced flow distortion at $f_r > 3$ only, which for $\overline{u} = 10\,\mathrm{m\,s^{-1}}$ and $z = 60$ m corresponds to $f = 0.5$ Hz, i.e. above the lowest eigenfrequencies of the Lysefjord bridge. At lower frequencies, the PSD estimates on H08 Wt and H08Wb show significant discrepancies with the one estimated from H08E, assumed representative of undisturbed flow conditions.

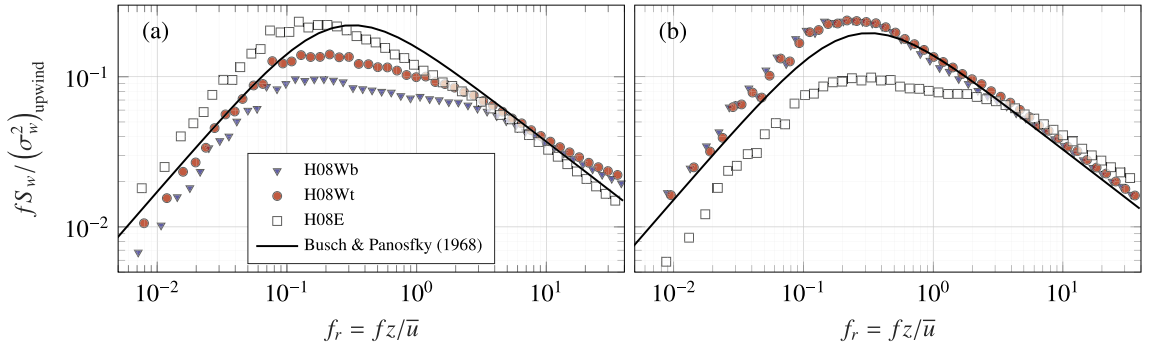

Fig. 11. (a) Vertical velocity spectra estimated on hangers 08 for a north-northeast flow (436 samples). (b) Vertical velocity spectra estimated on hangers 08 for a flow from south-southwest (415 samples).

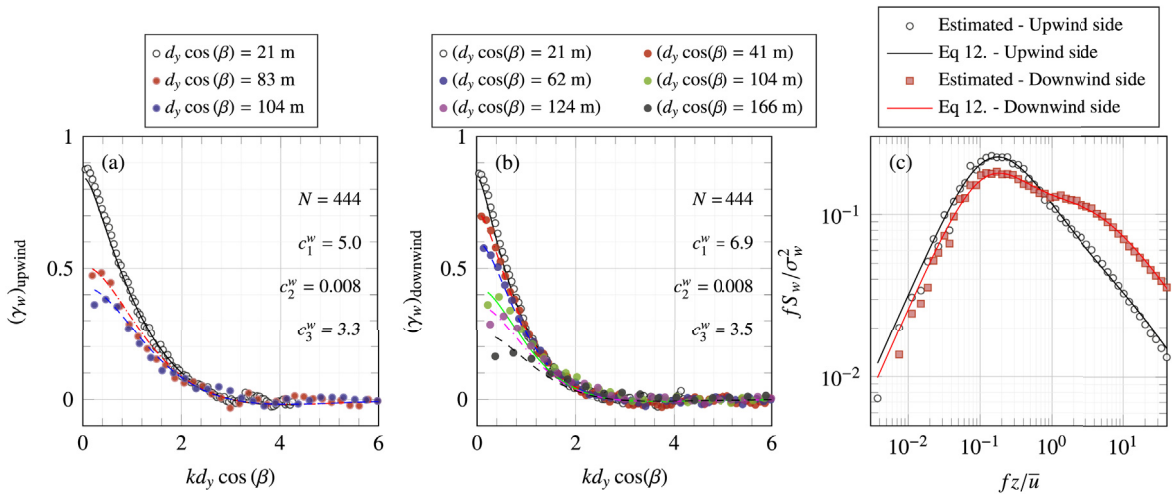

Fig. 12. Estimated (scatter plot) and modelled (solid lines) co-coherence estimate (a–b) and one-point PSD estimate (c) of the vertical wind component for a flow from north-northeast, using velocity records from July 2017 to May 2018.

A viable strategy to reduce deck-induced flow distortion is, therefore, to use anemometers on both sides of the girder, at a height corresponding to several deck heights. Flow distortion effects may also be expected in the measurement signal if the anemometers are installed on horizontal booms at the deck height. This was for example done by Xu and Zhu [8], who used 9m-long booms mounted perpendicularly to a 41 m-wide deck. Using their fitted spectral model, the computed ratio S_w/S_u converges toward 0.7 in the inertial subrange, compared to 1.33 following local isotropy. The results displayed in section 3 corroborate also those from Hay [3], which showed that mounting a sonic anemometer at the centre of a deck (with a height $H = 3.2$ m and width $B = 31$ m), even at a height of several meters above the road, should be avoided as flow distortion from every direction can be expected.

4. Wind-induced response of the Lysefjord bridge

4.1. Influence of model updating using improved data on the computed bridge response

The turbulence characteristics displayed in section 3 show that the underestimation of the vertical bridge response observed in Cheynet et al. [28] may be explained by the combination of girder-induced flow distortion and an incomplete anemometer calibration. The increased number of wind sensors and improved data post-processing allow, therefore, the modelling of an appropriate site-specific spectral model, summarized in Fig. 12. In this figure, the characteristics of both the one-point and two-point spectra are summarized for a north-northeast flow. The left and middle panel show the estimated and fitted co-coherence of the w component on the upwind side or downwind side of the deck, respectively. We recall that the west side of the deck is instrumented with more anemometers than the east side, which explains why the coherence on the downstream side is displayed for a larger variety of spatial separation than upwind. Finally, the right panel of Fig. 12 corresponds to the estimated and fitted one-point velocity spectrum S_w at mid-span on both the upwind side and the downstream side of the girder. Note that the difference between the normalized PSD estimates for the downwind side in Figs. 11 and 12 are simply due to the fact that the latter figure shows the normalized spectra "as seen" by each sonic anemometer, whereas the former figure shows the spectra normalized by the variance of the "undisturbed" vertical velocity on the upwind side. The co-coherence is modelled using a least-square fit of eq. (15) to the full-scale co-coherence estimates. A similar procedure is done for the velocity spectrum S_w using eq. (12). Both eqs. (12) and (15) provide an excellent fit of the vertical velocity spectrum and the co-coherence, respectively. The corresponding parameters for both wind sectors studied are summarized in Table 4, although only the case of a flow from north-northeast is considered in the following to study the buffeting response of the bridge.

The variance of the vertical acceleration and displacement response of the Lysefjord bridge is computed in the frequency domain using the wind load parameters displayed in Fig. 12 for different mean wind speeds and in the case of a north-northeast flow. This way, the influence of sensor position (upwind or downwind) on the computed bridge response is directly visualized. The computational responses are compared to full-scale measurements in Fig. 13, which correspond to the 30min acceleration records collected from July 2017 to May 2018.

Fig. 13 suggests that the site-specific spectral model designed using the wind measurements on the upwind side of the deck leads to slightly conservative estimates for both the acceleration and displacement response. If the wind data on the downwind side are used, the computed acceleration response of the bridge agrees well with the measured one but underestimates the real one if the displacement response is considered. These results infer that the use of an aerodynamic admittance equal to unity at every frequency may not be appropriate for the study of the wind-induced bridge acceleration response. Note that the

Table 4
Coefficients of the co-coherence (c_1, c_2, c_3) and one-point spectrum model (a_1, b_1, a_2, b_2) of the vertical wind velocity component, fitted in the least-square sense on the upwind and downwind side of the deck, for the two main wind direction recorded on the Lysefjord bridge.

Wind Direction	girder side	Co-coherence			One-point spectrum			
		c_1	c_2	c_3	a_1	b_1	a_2	b_2
North-northeast	Upwind	5.0	0.008	3.3	0.005	0.2	3.2	27.8
	Downwind	6.9	0.008	3.5	0.1	0.5	2.5	31.5
South-Southwest	Upwind	3.9	0.011	5.2	≈ 0	–	2.3	14.8
	Downwind	5.2	0.011	5.7	0.07	0.4	1.7	13.6

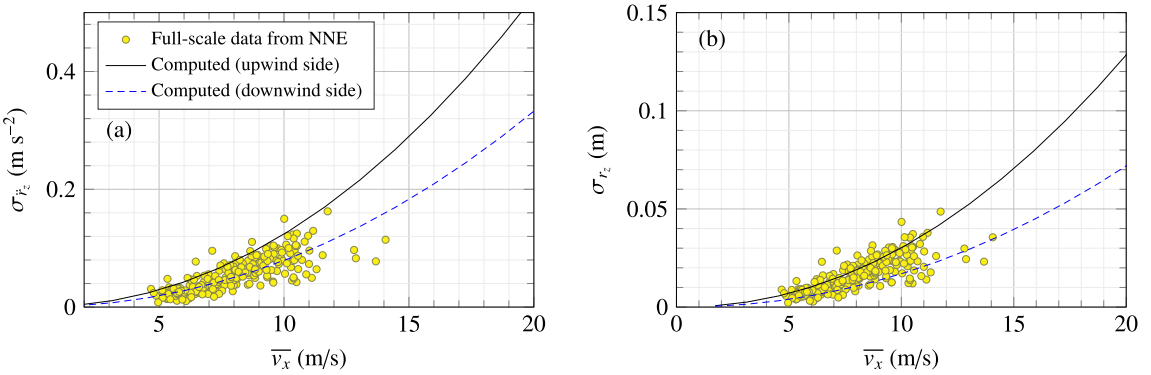

Fig. 13. Computed and estimated standard deviation of the vertical bridge acceleration (a) and displacement (b) responses at mid-span using the data recorded from July 2017 to May 2018 for a flow from north-northeast.

displacement response has been high-pass filtered to remove the spurious low-frequency component, which comes from the limited performances of the accelerometers at low frequencies. The filter applied is a 5th order Butterworth filter with a cut-off frequency at 0.05 Hz.

4.2. Improved wind load model based on a modified cross-sectional admittance function

The strip theory assumes, in its basic form, that the wind field across the bridge is not significantly affected by the presence of the deck so that the span-wise coherence of wind forces is equal to that of the undisturbed turbulence. An extended model includes a cross-sectional admittance function, accounting for turbulence "averaging" across the bridge deck as a function of the reduced frequency, $K = fB/\overline{u}$. In Larose [43], the significance of the turbulence integral length scale relative to the deck width L_w/B on the lift force characteristics was demonstrated, using the cross-sectional admittance function as well as the span-wise lift coherence. The latter was observed to be higher than the coherence of the vertical turbulence, in line with the findings in Jakobsen [44], Larose et al. [45], Matsuda et al. [46].

The discussion on flow distortion in section 3 indicates a non-negligible influence of the structure on the oncoming flow. In the following, the comparison between the computed and the recorded vertical bridge response is utilized to study the cross-sectional admittance function in full-scale. The computed response is based on the assumption that the horizontal wind velocity components have a negligible influence on the vertical buffeting response, and that the span-wise coherence of the vertical turbulence, available from the measurements, is representative of the coherence of the lift-force.

In full-scale studies, the approximation of a cross-sectional admittance function set equal to 1 for all frequencies ($\chi_w \approx 1$) is commonly adopted. If the bridge displacement response is considered and if its most significant eigenfrequencies are well below 1 Hz, the approximation $\chi_w \approx 1$ is generally found acceptable. However, if the acceleration response is used, the approximation $\chi_w \approx 1$ may no longer be valid, which appears to be the case of the Lysefjord bridge. This is shown in Fig. 14, where the acceleration and displacement spectra of the Lysefjord bridge vertical response is estimated at mid-span using a 1-h record duration on 21-11-2017 from 23:00, with a stationary mean wind speed of 10 ms^{-1} and a flow from north-northeast. It is clearly seen that the use of $\chi_w \approx 1$ hampers the proper decay of the acceleration response spectra with increased frequency of vibration, and thereby the overall acceleration response is overestimated.

The choice of using a simple cross-sectional aerodynamic admittance function for the Lysefjord bridge is not straightforward as the deck is somewhat bluff and, therefore, the Liepmann approximation of the Sears function [47] is not necessarily suitable. For a closed-box girder with a ratio $H/B > 5$ and $0.2 < L_w/B < 2$, Larose [43] proposed an empirical model that is an explicit function of both K and L_w/B. In Fig. 14, $L_w/B \approx 4$ and $H/B = 4.5$, which is beyond the scope of application for the model proposed by Larose [43]. If the latter model is used, the acceleration response is underestimated. A simpler, but still suitable,

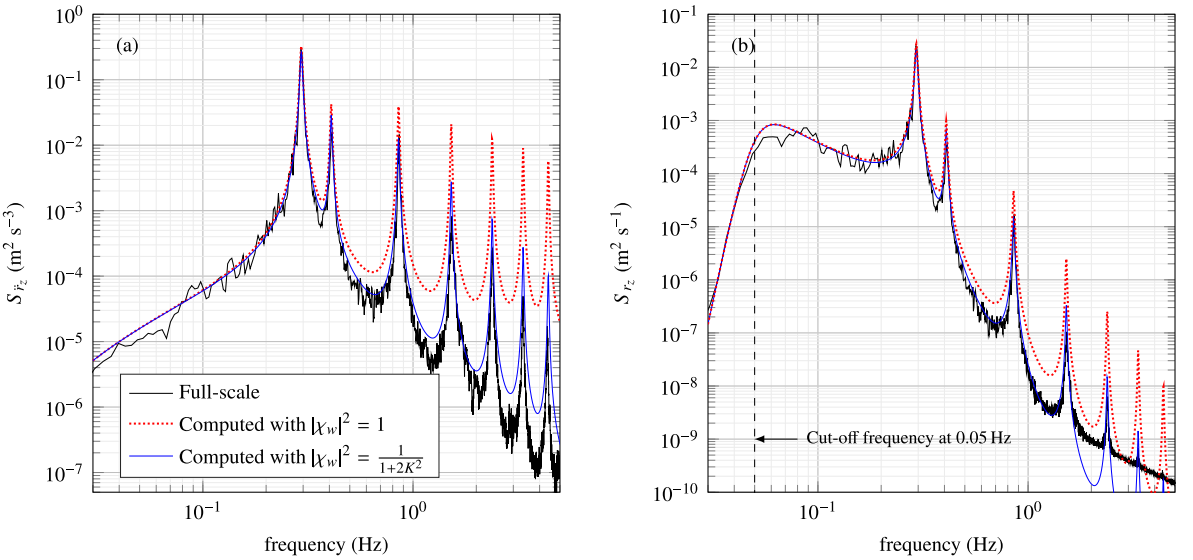

Fig. 14. Full-scale 1-h acceleration (a) and displacement (b) spectrum of the Lysefjord bridge on 21-11-2017 superposed to the computed ones, which have been obtained using the spectral velocity model displayed in Fig. 12 (upwind side) and different cross-sectional aerodynamic admittance functions.

cross-sectional admittance function for the Lysefjord bridge can be defined as a second-order low-pass filter, independent of L_w/B, with a cut-off frequency at $K \approx 0.45$,

$$|\chi_w(K)|^2 = \frac{1}{1+aK^2} \tag{20}$$

where $a = 2$ is a parameter empirically estimated based on the spectra of the recorded vertical acceleration response. The application of eq. (20) as a cross-sectional admittance function leads to an excellent agreement between the computed and full-scale acceleration spectra in Fig. 14. As expected, the use of eq. (20) as a cross-sectional admittance function has a much smaller influence on the computed bridge displacement response than on the acceleration response. Although it might be a coincidence, eq. (20) with $a = 2$ is identical to the expression proposed by Hansen et al. [48] in the design basis of the Hardanger Bridge, which was modelled with a hexagonal closed box-girder with a ratio $B/H = 5.5$.

Even if the parameter $a = 2$ in eq. (20) is established using only 1 h of high-quality data, Fig. 15 demonstrates that it greatly improves the agreement between the computed and estimated bridge response for the eleven months of acceleration record from July 2017 to May 2018. In this figure, the acceleration and displacement response of the bridge is computed using the same spectral and coherence models (Fig. 12), established on the upwind side of the girder. Note that the buffeting theory predicts that the turbulence intensity and the yaw angle are major sources of variability of the buffeting response of a wind-sensitive structure. Therefore, these have been accounted for in each sample considered in Fig. 15. Other sources of discrepancies, such as the variation of the bridge deck aerodynamic coefficients with the yaw angle [49], the limited validity of the quasi-steady theory as well as the contribution of the bridge towers and main cables to aerodynamic loading [50] are not included herein for

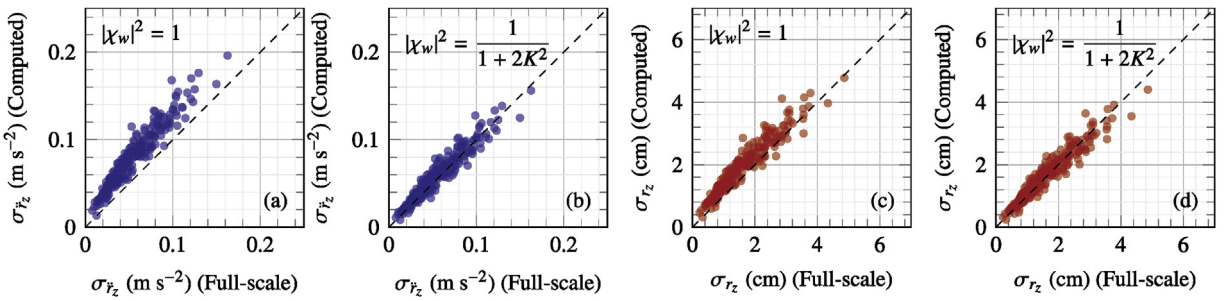

Fig. 15. Standard deviation of the vertical acceleration (a–b) and displacement response (c–d) of the bridge at mid-span using full-scale data from July 2017 to May 2018 (horizontal axis) and a computational model (vertical axis) relying on the spectral velocity model recorded on the upwind side and two different cross-sectional admittance functions χ_w.

the sake of simplicity. Finally, it should be noted that the results shown in Fig. 15 are consistent with those displayed in Figs. 13 and 14, where the use of eq. (20) as a cross-sectional admittance function has a much more visible effect on the acceleration response than on the displacement response.

5. Conclusions

Eleven months of wind velocity data collected by sonic anemometers mounted above the deck of a suspension bridge crossing the inlet of a fjord in south-western Norway have been studied. The complexity of the recorded flow is augmented by distortions caused by the bridge girder and the mountainous surroundings, as well as imperfections in the anemometer setup. Using an improved and extended bridge instrumentation as well as a rigorous data post-processing focusing on high-quality data only, the different sources of flow distortion have been identified, leading to the following findings:

- The vertical velocity component w recorded on the downstream side of the deck is underestimated because of deck-induced flow distortion. On the other hand, the two horizontal wind components u and v are much more affected by the terrain than by the girder. Consequently, the turbulence characteristics established for both a wind blowing from south-southwest and north-northeast can greatly deviate from the case of flat and homogeneous terrain. In particular, the ratio σ_w/σ_u might be as high as 0.7 in a narrow fjord whereas in flat and homogeneous terrain $\sigma_w/\sigma_u \approx 0.5$. For the two main wind directions considered, the flow is not affected the same way by the topography, which reinforces the idea that turbulence characteristics observed on a bridge crossing a fjord or a canyon should be studied separately for different sectors.
- For a hexagonal girder with a width to height ratio $B/H \approx 4.5$, mounting a sonic anemometer at a height equal to $3.6H$ above the deck instead of $2.2H$ shows only minor improvements in flow distortion mitigation if located downwind. To study turbulence characteristics from a long-span bridge, it is thus advised to mount sonic anemometers on both sides of the girder. Such an installation is particularly important in a mountainous area where the characterization of the wind conditions needs to be conducted after separation of the records in different wind sectors, where some of the anemometers will inevitably be located on the downstream side of the deck.
- If the wind velocity measurements are conducted on the downstream side of the deck, the wind load is substantially underestimated, compared to measurements on the upstream side, which are affected to a lower degree by the flow disturbance of the bridge deck. The bridge response estimation is, however, observed to be sensitive to the bridge cross-sectional admittance applied. Assuming a simple admittance function equal to unity at every frequency will result in an overestimated response when used with wind data measured upstream, but may lead to a reasonable agreement between computed and recorded response when used with wind data measured downstream. However, it is shown herein that modelling the admittance function as a simple second order filter will lead to a significantly improved agreement between the computed and observed full-scale bridge response when used in combination with wind load information collected on the upwind side of the deck.

Acknowledgements

The support of the Norwegian Public Roads Administration to develop the bridge monitoring system is gratefully acknowledged, as well as their assistance during the installation and maintenance of the system.

References

[1] N. Jensen, E. Hjort-Hansen, Dynamic Excitation of Structures by Wind-Turbulence and Response Measurements at the Sotra Bridge, Tech. Rep. Report No. STF71 A., SINTEF, 1977.
[2] L. Kristensen, N.O. Jensen, Lateral coherence in isotropic turbulence and in the natural wind, Boundary-Layer Meteorol. 17 (3) (1979) 353–373.
[3] J.S. Hay, Analyses of wind and response data from the Wye and Erskine Bridges and comparison with theory, J. Wind Eng. Ind. Aerod. 17 (1) (1984) 31–49.
[4] J. Bietry, D. Delaunay, E. Conti, Comparison of full-scale measurement and computation of wind effects on a cable-stayed bridge, J. Wind Eng. Ind. Aerod. 57 (2) (1995) 225–235.
[5] R. Toriumi, H. Katsuchi, N. Furuya, A study on spatial correlation of natural wind, J. Wind Eng. Ind. Aerod. 87 (2) (2000) 203–216.
[6] T. Miyata, H. Yamada, H. Katsuchi, M. Kitagawa, Full-scale measurement of Akashi–Kaikyō bridge during typhoon, J. Wind Eng. Ind. Aerod. 90 (12) (2002) 1517–1527.
[7] J.H. Macdonald, Evaluation of buffeting predictions of a cable-stayed bridge from full-scale measurements, J. Wind Eng. Ind. Aerod. 91 (12) (2003) 1465–1483.
[8] Y. Xu, L. Zhu, Buffeting response of long-span cable-supported bridges under skew winds. Part 2: case study, J. Sound Vib. 281 (3) (2005) 675–697.
[9] J.S. Hay, The Wind-Induced Response of the Erskine Bridge, chap. 6, ICE publishing, 1981, pp. 81–90.
[10] J. Frandsen, Simultaneous pressures and accelerations measured full-scale on the Great Belt East suspension bridge, J. Wind Eng. Ind. Aerod. 89 (1) (2001) 95–129.
[11] J.T. Snæbjörnsson, J.B. Jakobsen, E. Cheynet, J. Wang, Full-scale monitoring of wind and suspension bridge response, IOP Conf. Ser. Mater. Sci. Eng. 276 (1) (2017) 012007.
[12] T. Nakai, M. Van der Molen, J. Gash, Y. Kodama, Correction of sonic anemometer angle of attack errors, Agric. For. Meteorol. 136 (1–2) (2006) 19–30.
[13] T. Nakai, K. Shimoyama, Ultrasonic anemometer angle of attack errors under turbulent conditions, Agric. For. Meteorol. 162 (2012) 14–26.
[14] D. Vickers, L. Mahrt, Quality control and flux sampling problems for tower and aircraft data, J. Atmos. Ocean. Technol. 14 (3) (1997) 512–526.
[15] I. Stiperski, M.W. Rotach, On the measurement of turbulence over complex mountainous terrain, Boundary-Layer Meteorol. 159 (1) (2016) 97–121.
[16] K.T. Paw U, D.D. Baldocchi, T.P. Meyers, K.B. Wilson, Correction of eddy-covariance measurements incorporating both advective effects and density fluxes, Boundary-Layer Meteorol. 97 (3) (2000) 487–511.
[17] J.M. Wilczak, S.P. Oncley, S.A. Stage, Sonic anemometer tilt correction algorithms, Bound-Layer Meteorol. 99 (1) (2001) 127–150.

[18] R.T. McMillen, An eddy correlation technique with extended applicability to non-simple terrain, Boundary-Layer Meteorol. 43 (3) (1988) 231–245.
[19] C. Klipp, Turbulent friction velocity calculated from the Reynolds stress tensor, J. Atmos. Sci. 75 (4) (2018) 1029–1043.
[20] M. Shinozuka, G. Deodatis, Simulation of stochastic processes by spectral representation, Appl. Mech. Rev. 44 (4) (1991) 191–204.
[21] R. Weber, Remarks on the definition and estimation of friction velocity, Boundary-Layer Meteorol. 93 (2) (1999) 197–209.
[22] F.T. Nieuwstadt, The turbulent structure of the stable, nocturnal boundary layer, J. Atmos. Sci. 41 (14) (1984) 2202–2216.
[23] Z. Sorbjan, On similarity in the atmospheric boundary layer, Boundary-Layer Meteorol. 34 (4) (1986) 377–397.
[24] P.D. Welch, The use of fast Fourier transform for the estimation of power spectra: a method based on time averaging over short, modified periodograms, IEEE Trans. Audio Electroacoust. 15 (1967) 70–73.
[25] A. Davenport, The buffeting of large superficial structures by atmospheric turbulence, Ann. N. Y. Acad. Sci. 116 (1) (1964) 135–160.
[26] R. Scanlan, The action of flexible bridges under wind, II: buffeting theory, J. Sound Vib. 60 (2) (1978) 201–211.
[27] E. Cheynet, Wind-induced Vibrations of a Suspension Bridge: A Case Study in Full-Scale. (Ph.D. thesis), University of Stavanger, Norway, 2016.
[28] E. Cheynet, J.B. Jakobsen, J. Snæbjörnsson, Buffeting response of a suspension bridge in complex terrain, Eng. Struct. 128 (2016) 474–487.
[29] J. Xie, H. Tanaka, R. Wardlaw, M. Savage, Buffeting analysis of long-span bridges to turbulent wind with yaw angle, J. Wind Eng. Ind. Aerod. 37 (1) (1991) 65–77.
[30] K. Saranyasoontorn, L. Manuel, P.S. Veers, A comparison of standard coherence models for inflow turbulence with estimates from field measurements, J. Sol. Energy Eng. 126 (4) (2004) 1069–1082.
[31] R. Sigbjörnsson, E. Hjorth-Hansen, Along-wind response of suspension bridges with special reference to stiffening by horizontal cables, Eng. Struct. 3 (1) (1981) 27–37.
[32] E.N. Strømmen, Structural Dynamics; Chap. Eigenvalue Calculations of Continuous Systems, Springer International Publishing, Cham, 2014, ISBN: 978-3-319-01802-7, pp. 89–159, https://doi.org/10.1007/978-3-319-01802-7_3.
[33] F. Magalhães, A. Cunha, E. Caetano, Online automatic identification of the modal parameters of a long-span arch bridge, Mech. Syst. Signal Process. 23 (2) (2009) 316–329, https://doi.org/10.1016/j.ymssp.2008.05.003.
[34] A.G. Davenport, The spectrum of horizontal gustiness near the ground in high winds, Q. J. R. Meteorol. Soc. 87 (372) (1961) 194–211, https://doi.org/10.1002/qj.49708737208.
[35] K. Harstveit, Full-scale measurements of gust factors and turbulence intensity, and their relations in hilly terrain, J. Wind Eng. Ind. Aerod. 61 (2–3) (1996) 195–205.
[36] E. Cheynet, J.B. Jakobsen, J. Snæbjörnsson, J. Reuder, V. Kumer, B. Svardal, Assessing the potential of a commercial pulsed lidar for wind characterisation at a bridge site, J. Wind Eng. Ind. Aerod. 161 (2017) 17–26.
[37] M. De Franceschi, D. Zardi, M. Tagliazucca, F. Tampieri, Analysis of second-order moments in surface layer turbulence in an Alpine valley, Q. J. R. Meteorol. Soc. 135 (644) (2009) 1750–1765.
[38] G. Solari, G. Piccardo, Probabilistic 3-D turbulence modeling for gust buffeting of structures, Probabilist. Eng. Mech. 16 (1) (2001) 73–86.
[39] J.C. Kaimal, J. Wyngaard, Y. Izumi, O. Coté, Spectral characteristics of surface-layer turbulence, Q. J. R. Meteorol. Soc. 98 (417) (1972) 563–589.
[40] N.E. Busch, H.A. Panofsky, Recent spectra of atmospheric turbulence, Q. J. R. Meteorol. Soc. 94 (400) (1968) 132–148.
[41] J. Hunt, J. Graham, Free-stream turbulence near plane boundaries, J. Fluid Mech. 84 (2) (1978) 209–235.
[42] A.N. Kolmogorov, The local structure of turbulence in incompressible viscous fluid for very large Reynolds numbers, Dokl. Akad. Nauk SSSR 30 (1941) 299–303.
[43] G.L. Larose, The spatial distribution of unsteady loading due to gusts on bridge decks, J. Wind Eng. Ind. Aerod. 91 (12–15) (2003) 1431–1443.
[44] J.B. Jakobsen, Span-wise structure of lift and overturning moment on a motionless bridge girder, J. Wind Eng. Ind. Aerod. 69 (1997) 795–805.
[45] G. Larose, H. Tanaka, N. Gimsing, C. Dyrbye, Direct measurements of buffeting wind forces on bridge decks, J. Wind Eng. Ind. Aerod. 74 (1998) 809–818.
[46] K. Matsuda, Y. Hikami, T. Fujiwara, A. Moriyama, Aerodynamic admittance and the strip theory' for horizontal buffeting forces on a bridge deck, J. Wind Eng. Ind. Aerod. 83 (1–3) (1999) 337–346.
[47] H. Liepmann, On the application of statistical concepts to the buffeting problem, J. Aeronaut. Sci. 19 (12) (1952) 793–800.
[48] S. Hansen, M. Lollesgaard, S. Rex, J. Jakobsen, E. Hjorth-Hansen, The Hardanger Bridge: Static and Dynamic Wind Tunnel Tests with a Section Model. Prepared for the Norwegian Public Roads Administration, Tech. Rep. Revision 1, Svend Ole Hansen ApS., 2006.
[49] L. Zhu, Y. Xu, F. Zhang, H. Xiang, Tsing Ma bridge deck under skew winds—part I: aerodynamic coefficients, J. Wind Eng. Ind. Aerod. 90 (7) (2002) 781–805.
[50] J. Wang, E. Cheynet, J.B. Jakobsen, J. Snæbjörnsson, Time-domain analysis of wind-induced response of a suspension bridge in comparison with the full-scale measurements, in: ASME 2017 36th International Conference on Ocean, Offshore and Arctic Engineering, Trondheim, Norway, American Society of Mechanical Engineers, 2017, p. V03BT02A032–V03BT02A032.